Journal homepage http://revistas.unitru.edu.pe/index.php/SSMM

SELECCIONES MATEMÁTICAS
Universidad Nacional de Trujillo
ISSN: 2411-1783 (Online)
2025; Vol.12(2):261-272.

Special issue: XII International Congress of Applied and Computational Mathematics

Numerical Modeling and Simulations for an Ocean Circulation Model of the Southern Pacific

Thomas Hartmann, Ernst P. Stephan and Thomas Wick

Received, May. 22, 2025; *Accepted, Oct. 30, 2025;* *Published, Dec. 27, 2025*

How to cite this article:
Hartmann T. et al. *Numerical Modeling and Simulations for an Ocean Circulation Model of the Southern Pacific*. Selecciones Matemáticas. 2025;12(2):261–272. https://doi.org/10.17268/sel.mat.2025.02.01

Abstract

In this work, we consider the primitive equations of an ocean circulation model for the southern pacific, which consists of the time-dependent Navier-Stokes equations in the β-plane coupled with the temperature transport equation. Specifically, the full three-dimensional equations are adopted and formulated as a monolithic system of nonstationary, nonlinear, coupled partial differential equations. The El Niño phenomenon is simulated by the action of given wind stresses on the ocean surface. We present an approximation scheme with Crank-Nicolson finite differences in time, and in space we take inf-sup stable Galerkin finite elements for the Navier-Stokes part and bilinear elements for the temperature. We solve the resulting, nonlinear monolithic discrete system by Newton´s method. Numerical experiments with realistic geometry and material data are conducted, which show the practicability of our approach.

Keywords . Navier-Stokes equations, Temperature model, Monolithic approach, Galerkin finite elements, El Niño

1. Introduction. This work is devoted to numerical modeling and simulations of the ocean circulation in the southern pacific; see e.g. [1, 2]. In that part of the ocean, an important phenomenum is El Niño, which is a non-cyclic, change of sea currents. It appears in non-regular intervals of 4 years in average. During El Niño warm surface waters appear for several months over the entire equatorial zone in the Pacific. Europe is interfered of a similar phenomena in the Atlantic with strong influence on the European weather. We consider the model for circulation of tropical ocean when El Niño appears. The ocean current is described by the primitive equations which consist of the equations of motion and temperature transport which are strongly coupled. The wind stresses on the surface of the ocean are fundamental for the warming of waters.
The warm tropical oceans are fundamental in regulating Earth's climate and driving large-scale weather phenomena, such as monsoons, tropical cyclones, and El Niño-Southern Oscillation (ENSO) events. Among these, the equatorial oceans are particularly critical due to their heightened sensitivity to atmospheric forces, which result in rapid oceanic responses. This makes them ideal for studying dynamic oceanic motions on monthly or longer time scales, see [3].

However, the limited availability of in-situ observations, combined with the complex interactions between the ocean and atmosphere in these regions, underscores the need for accurate and reliable models. These models are crucial for simulating equatorial wave motions, see [4, 5], and

*Technische Hochschule Ulm, Germany. (Thomas.Hartmann@thu.de).
†Leibniz Universität Hannover, Germany. (stephan@ifam.uni-hannover.de).
‡Leibniz Universität Hannover, Germany. (thomas.wick@ifam.uni-hannover.de).

are vital for improving our understanding of global climate variability and enhancing weather and climate prediction systems.

The objective of this work is the design of a robust numerical approach for three-dimensional simulations of a simplified ocean circulation model. Specifically, the incompressible Navier-Stokes equations are coupled to a temperature equation, a so-called Boussinesq approximation. The equation of state for the density and the salinity approximation are neglected. For such models, we refer to [6]. The three-dimensional model (in comparison to homogenized models such as [6, 7]) allows for an easy access of flow and temperature values in intermediate ocean levels for $(-d, 0)$, where $-d$ is the ocean depth. The Navier-Stokes temperature model is formulated as a monolithic system resulting into a nonstationary, nonlinear, coupled PDE system. This system is discretized with the Rothe method, namely a One-Step-θ scheme in time and Galerkin finite elements in space. Newton's method is employed for the nonlinear solution. The implementation is done in the modern open-source finite element library deal.II [8] using the multiphysics template [9]. Different boundary conditions on the ocean surface for the wind stress, i.e., Neumann conditions for the Navier-Stokes part, are used.

The outline of this paper is as follows. In Section 2 the modelling equations in the β-plane are introduced together with the boundary conditions and initial conditions. Then the corresponding variational formulation is given. Next, in Section 3 the discretization in space and time is performed. Moreover, the nonlinear and linear solution schemes are briefly explained. Finally, in Section 4, some numerical simulations are carried out with underline the relevance of our approach.

2. Modeling.

Our model is inspired by [6] and [7], but we fully stay in three dimensions without averaging in the vertical direction. However, the salinity and variable density are omitted, resulting into a simplified model system. Nonetheless, the system remains a challenging nonstationary, nonlinear, coupled PDE system, where the numerical solution is costly due to the big dimensions, 3D-setting, and the choices of the numerous parameters.

2.1. Notation.

Let $\Omega \subset \mathbb{R}^3$ be sufficiently smooth and let $I := (0, T)$ with $T > 0$ be some time interval. More specifically, let

$$\Omega = (0, L_1) \times (-D, D) \times (-h, 0).$$

The specific values are provided below in Table 4.1.

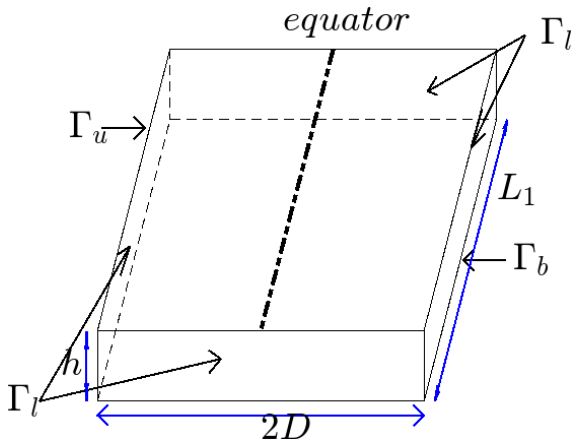

Figure 2.1: Sketch of the domain and the boundaries.

2.2. Equations.

Find vector-valued velocities $v = (v_x, v_y, v_z) : \Omega \times I \to \mathbb{R}^3$, scalar-valued pressure $p : \Omega \times I \to \mathbb{R}$, scalar-valued temperature $\vartheta : \Omega \times I \to \mathbb{R}$ such that

$$\begin{aligned} &\rho\, \partial_t v + \rho(v \cdot \nabla)v - \nabla \cdot (\rho\nu(\nabla v + \nabla v^T)) \\ &+\nabla p + (0, 0, \rho g)^T + \alpha\beta\, \nabla\vartheta + \frac{1}{R_0} 2\cos(\Theta) k \times v = 0 \quad \text{in } \Omega \times I, \qquad (2.1) \\ &\nabla \cdot v = 0 \quad \text{in } \Omega \times I, \qquad (2.2) \\ &\partial_t \vartheta + (v \cdot \nabla)\vartheta - \nabla \cdot (\kappa \nabla \vartheta) = 0 \quad \text{in } \Omega \times I. \qquad (2.3) \end{aligned}$$

Here, $k = (k_x, k_y, k_z) = (0, 0, 1)^T$, i.e.,

$$k \times v = \begin{pmatrix} 0 \\ 0 \\ 1 \end{pmatrix} \times \begin{pmatrix} v_x \\ v_y \\ v_z \end{pmatrix} = \begin{pmatrix} -v_y \\ v_x \\ 0 \end{pmatrix},$$

with density ρ, kinematic viscosity ν, thermal coefficient α, colatitude Θ (the colatitude is computed as $\Theta = \arcsin(y/a)$, where $(x, y, z) \in \Omega$ and a is the Earth radius), coefficient β [10][p.624], and the Rossby number R_0. Moreover, $\nu > 0$ is the kinematic viscosity:

$$\nu := \begin{pmatrix} \nu_x & 0 & 0 \\ 0 & \nu_y & 0 \\ 0 & 0 & \nu_z \end{pmatrix}.$$

In the temperature part, $\kappa > 0$ is the thermal expansion coefficient.

2.3. Boundary conditions. We recall that the boundary is split into

$$\partial\Omega = \Gamma_u \cup \Gamma_b \cup \Gamma_l, \tag{2.4}$$

where Γ_u is the upper (top) boundary at sea level, Γ_b the bottom of the ocean, and Γ_l all surrounding (side) boundaries. The following boundary conditions are prescribed:

$$\begin{aligned} \partial_z(v_x, v_y) = \bar{\tau} = (\tau^x, 0) &\quad \text{on } \Gamma_u \times I \qquad (2.5)\\ v_z = 0 &\quad \text{on } \Gamma_u \times I \\ \partial_z \vartheta = 10^{-5}\gamma(\vartheta_A - \vartheta) &\quad \text{on } \Gamma_u \times I \\ v = (v_x, v_y, v_z) = 0 &\quad \text{on } \Gamma_b \times I \qquad (2.6)\\ \vartheta = 4^\circ &\quad \text{on } \Gamma_b \times I \\ v = (v_x, v_y, v_z) = 0 &\quad \text{on } \Gamma_l \times I \qquad (2.7)\\ \partial_{\vec{n}} \vartheta = 0 &\quad \text{on } \Gamma_l \times I. \end{aligned}$$

The main driving mechanisms are τ^x for the Navier-Stokes system and $10^{-5}\gamma(\vartheta_A - \vartheta)$ for the temperature system. For the calculation of τ^x we consider two cases.

Case 1. Here, we follow [11]. The zonal trade winds is composed by two patches

$$\tau^x = \begin{cases} \tau_1 = \tau_W + \tau_H, & \vartheta < \vartheta_m \\ \tau_2 = \tau_H, & \vartheta_m \leq \vartheta \end{cases}, \tag{2.8}$$

where ϑ is evaluated at $(L_1, 0, 0)$, that is the east part at the Peruvian coast.

Moreover,

$$\begin{aligned} \tau_W &= \tau_{ow} X(x) Y(y) \qquad (2.9)\\ \tau_H &= \tau_{oh} X(x) Y(y) * 10^6 * \sin(4.0\pi t / 8\,640\,000) \end{aligned}$$

where t is the time in seconds, and the end time $T = 50$ days and,

$$\begin{aligned} \tau_{ow} &= -0.05 Nm^{-2}, \\ \tau_{oh} &= 0.015 Nm^{-2}, \\ \lambda &= 3000km \quad [11], \text{p.349} \\ X(x) &= \cos\left(\frac{2\pi}{L_1}(x - \frac{L_1}{2})\right), \quad \frac{L_1}{4} < x < \frac{3L_1}{4}, \\ Y(y) &= \frac{1}{2}\left(1 + \cos\left(\frac{2\pi}{\lambda} y\right)\right), \quad |y| < \lambda, \\ X = Y &= 0 \quad \text{otherwise.} \end{aligned}$$

We notice that τ_H differs from [11] and has been scaled with 10^6 in order to observe more significantly the effects of the wind stress. To employ the original wind stress proposed by [11] is ongoing work.

Case 2. As Case 1, but now we set $T = 365$ days and used a modified wind stress.

$$\tau_W = \tau_{ow} X(x) Y(y), \tag{2.10}$$
$$\tau_H = \tau_{oh} X(x) Y(y) * 10^6 * \sin(4.0\pi t/63\,072\,000).$$

In both cases, the patch τ_H of the wind stress is one oscillation of a sine function, that is, it starts with zero, it increases, then decreases, switches to negative values and ends with zero.

2.4. Initial conditions. Moreover, as initial conditions, we prescribe

$$v(0) = v_0 \quad \text{in } \Omega \times \{0\}, \tag{2.11}$$
$$\vartheta(0) = \vartheta_0 \quad \text{in } \Omega \times \{0\}. \tag{2.12}$$

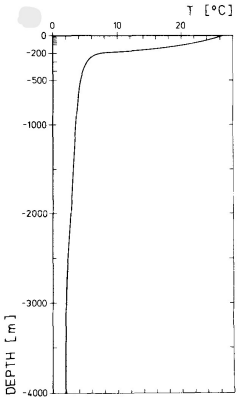

Figure 2.2: Temperature profile $\vartheta(0)$; see [12], where this figure is taken from.

For ϑ_0, the temperature profile of [12] is applied with appropriate interpolation in the z direction. We note that the initial temperature must be compatible (having the same values) with the temperature boundary conditions.

2.5. Weak formulation. The weak forms are as follows. For the Navier-Stokes system, we have: Find $U = (v, p, \vartheta) \in H^1(I, V^v) \times L^2(I, V^p) \times L^2(I, V^\vartheta)$, where

$$V^v := \{u \in H^1(\Omega)^d |\ u_z = 0 \text{ on } \Gamma_u, u = 0 \text{ on } \Gamma_b \cup \Gamma_l\}, \tag{2.13}$$
$$V^\vartheta := \{\chi \in H^1(\Omega) |\ \chi = 0 \text{ on } \Gamma_b\} \tag{2.14}$$

and $V^p := L^2(\Omega)$ such that

$$\begin{aligned} A_{v,p,\vartheta}(U)(\Psi) := &\int_I \int_\Omega \rho \partial_t v \cdot \psi^v \, dV \, dt + \int_I \int_\Omega \rho (v \cdot \nabla) v \cdot \psi^v \, dV \, dt \\ &+ \int_I \int_\Omega \rho \nu (\nabla v + \nabla v^T) : \nabla \psi^v \, dV \, dt - \int_I \int_{\Gamma_u} (\tau^x, 0)^T \cdot (\psi_x^v, \psi_y^v)^T \, ds \, dt \\ &+ \int_I \int_\Omega (\nabla p + (0, 0, \rho g)^T) \cdot \psi^v \, dV \, dt \quad + \alpha\beta \int_I \int_\Omega \nabla \vartheta \cdot \psi^v \, dV \, dt \\ &+ \int_I \int_\Omega \frac{1}{R_0} 2 \cos(\Theta)(k \times v) \cdot \psi^v \, dV \, dt \quad + \int_I \int_\Omega \nabla \cdot v \cdot \psi^p \, dV \, dt = 0, \end{aligned} \tag{2.15}$$

for all test functions $\Psi = (\psi^v, \psi^p)$ with $\psi^v = (\psi_x^v, \psi_y^v, \psi_z^v) \in L^2(I, V^v)$ and $\psi^p \in L^2(I, V^p)$. In addition, we used $dV := dxdydz$ as the volume increment. For the temperature equation, we have: Find $(\vartheta, v) \in H^1(I, \{\vartheta|_{\Gamma_b} = 4 + V^\vartheta\}) \times L^2(I, V^v)$, such that

$$\begin{aligned} A_{\vartheta,v}(\vartheta, v)(\psi^\vartheta) := &\int_I \int_\Omega \partial_t \vartheta \psi^\vartheta \, dV \, dt + \int_I \int_\Omega (v \cdot \nabla) \vartheta \psi^\vartheta \, dV \, dt \\ &+ \int_I \int_\Omega \alpha \nabla \vartheta \cdot \nabla \psi^\vartheta \, dV \, dt - \int_I \int_{\Gamma_u} 10^{-5} \gamma (\vartheta_A - \vartheta) \psi^\vartheta \, ds \, dt = 0, \end{aligned} \tag{2.16}$$

for all test functions $\psi^\vartheta \in L^2(I, V^\vartheta)$.

3. Discretization. In this section, we introduce temporal and spatial discretization. Then, the nonlinear and linear solution schemes are briefly explained.

3.1. Variational-monolithic formulation. The weak form is formulated as a volume-coupled variational monolithic system [13] [Section 3.3.1]. To this end, we have: Find $\tilde{U} = (v, p, \vartheta) \in H^1(I, V^v) \times L^2(I, V^p) \times H^1(I, V^\vartheta)$ such that

$$A\begin{pmatrix}\tilde{U}\\(v,\vartheta)\end{pmatrix}(\Psi) := \begin{pmatrix}A_{v,p,\vartheta}\\A_{\vartheta,v}\end{pmatrix}\begin{pmatrix}\tilde{U}\\(v,\vartheta)\end{pmatrix}(\Psi) = 0 \quad \forall \Psi = (\psi^v, \psi^p, \psi^\vartheta) \in L^2(I, V^0), \tag{3.1}$$

where $A_{v,p,\vartheta} = A_{v,p} + A_\vartheta$, $V := V^v \times V^p \times \{\vartheta|_{\Gamma_b} = 4 + V^\vartheta\}$ and $V^0 := V^v \times V^p \times V^\vartheta$.

This system is discretized with the help of the Rothe method: finite differences in time via the shifted Crank-Nicolson scheme and a Galerkin finite element discretization in space.

3.2. Finite differences in time. We apply a One-Step-θ scheme to

$$A(U)(\Psi) = 0.$$

For the θ it holds $\theta \in [0, 1]$ with $\theta = 0$ for the explicit Euler scheme and $\theta = 1$ for the implicit Euler scheme. We are specifically interested in $\theta + \Delta t$ (for $\Delta t \ll 1$), where $\Delta t = t_m - t_{m-1}$, which results in the so-called shifted Crank-Nicolson scheme, which is second order and strictly $A - stable$.

In more detail the backward Euler discretization with $\theta = 1$, reads: Given the previous time step solution U^{m-1}, find the current time step solution U^m, $m = 1, \ldots, M$, such that

$$\begin{aligned}
&\int_\Omega \rho\, \frac{v^m - v^{m-1}}{\Delta t} \cdot \psi^v \, dV + \int_\Omega \rho\, (v^m \cdot \nabla) v^m \cdot \psi^v \, dV \\
&+ \int_\Omega \sigma_v(v^m) : \nabla \psi^v \, dV - \int_{\Gamma_u} (\tau^{x,m}, 0)^T \cdot (\psi^v_x, \psi^v_y)^T \, ds \\
&+ \int_\Omega (\nabla p^m + (0, 0, \rho g)^T) \cdot \psi^v \, dV + \alpha\beta \int_\Omega \nabla \vartheta^m \cdot \psi^v \, dV \\
&+ \int_\Omega \frac{1}{R_0} 2\cos(\Theta)(k \times v^m) \cdot \psi^v \, dV + \int_\Omega \nabla \cdot v^m \psi^p \, dV \\
&+ \int_\Omega \frac{\vartheta^m - \vartheta^{m-1}}{\Delta t} \psi^\vartheta \, dV + \int_\Omega (v^m \cdot \nabla)\vartheta^m \psi^\vartheta \, dV \\
&+ \int_\Omega \alpha \nabla \vartheta^m \cdot \nabla \psi^\vartheta \, dV - \int_{\Gamma_u} \gamma(\vartheta_A - \vartheta^m)\psi^\vartheta \, ds = 0.
\end{aligned}$$

In abstract form, the time-discretized problem reads: Given $U^{m-1} \in V$, find $U^m \in V$ for $m = 1, \ldots, M$ such that

$$A(U^m)(\Psi) = 0 \quad \forall \Psi \in V.$$

More details on the schemes as well as the extension to Crank-Nicolson can be found in [13][Section 5.3]. We notice that we have implemented the backward Euler scheme and the Crank-Nicolson scheme (pure as well as shifted) in our programming code.

3.3. Fully discrete problem. By using finite element discretizations on hexahedra, with $(v^m, p^m, \vartheta^m)|_K \in Q^2 \times Q^1 \times Q^1$ and $(v^m, p^m, \vartheta^m) \in V_h$, we have in abstract fully discrete form: Given $U_h^{m-1} \in V_h$, find $U_h^m \in V_h$ for $m = 1, \ldots, M$ such that

$$A(U_h^m)(\Psi_h) = 0 \quad \forall \Psi_h \in V_h.$$

As finite element spaces, for the Navier-Stokes part, an inf-sup stable Taylor-Hood element Q^2/Q^1 is used; see e.g. [14]. The temperature part is solved with bilinear elements Q^1. More specifically, we employ isoparametric shape functions as follows: On the mesh $\mathcal{T}_h = \{K_o\}_{o=1}^O$, for O mesh elements, we employ a conforming finite element space $V_h^s \subset V$, where $V = H_0^1(\Omega)$ and $s \in \mathbb{N}_0$ is the polynomial degree. Then, we define

$$V_h := V_h^s := \{v \in V | v|_K \in Q^s(K) \text{ for } K \in \mathcal{T}_h\} = \{v_1, \ldots, v_N\}, \quad \dim(V_h) = N,$$

with shape functions from $Q^s(K)$. Let $\hat{K}$ be the reference element, e.g., $\hat{K} = (0, 1)^{\tilde{d}}$. In isoparametric finite elements, the space $Q^s(K)$ is obtained from $\hat{Q}^s(\hat{K})$ and where the transformation from $\hat{K} \to K$ is of the same polynomial type as $\hat{Q}^s(\hat{K})$, and where

$$\hat{Q}^s(\hat{K}) = \text{span}\left\{ \prod_{j=1}^{\tilde{d}} x_j^{\alpha_j} \mid \alpha_j \in \mathbb{N}_0, \quad \alpha_j \le s \right\}.$$

3.4. Nonlinear and linear solution. The resulting monolithic discretized system is nonlinear. Here, we employ a line-search Newton method in which the Jacobian is derived analytically by hand. Therein, in the defect step, the arising linear systems are solved with a sparse direct solver. The entire programming framework is based on an adaptation of the open-source multiphysics template [9], which is based on the open-source finite element library deal.II 9.6.0 [8]. The criterion for termination the Newton method is a relative residual less the 10^{-8}. In our calculations, the number of iterations for each solved system was smaller than 5, in most time points we observe 2 iterations.

4. Numerical Results. In this section, we conduct some numerical simulations. The ocean is modeled as a cuboid $\Omega \subset \mathbb{R}^3$ with realistic length, width, and depth scales. This leads to highly anisotropic finite element meshes. All parameters are listed in Table 4.1.

4.1. Geometry and parameters. In this section, we list all data in Table 4.1.

Parameter	Notation	Value
Time step size	Δt	86 400 s (=1 day)
Final time T	T	50 days / 160 days
Ocean length	L_1	14 000 km
Ocean width	D	3 300 km
Ocean depth	H	4 km
Earth radius	a	6371 km
Density	ρ	$10^3 kg/m^3$
Viscosity (horizontal)	A_V, i.e., ν_x and ν_y	$10^4 m^2/s$
Viscosity (vertical)	k_V, i.e., ν_z	$15 \times 10^{-4} m^2/s$
Gravity	g	$9.8 m/s^2$
Thermal expansion coefficient	α	$0.0003 C^{-1}$
Model parameter	β	$2 \times 10^{-11} m^{-1} s^{-1}$
Thermal transport coefficient	γ	$12.552 J/m^2 sK$
Rossby number	R_0	9.7656×10^{-4}
Thermal expansion coefficient	κ	0.0003
Temperature condition	ϑ_m	$20°C$
Temperature condition	ϑ_A	$26°C$

Table 4.1: Problem data.

In Figure 4.1, the three dimensional mesh with relatively small step size in z-direction is shown.

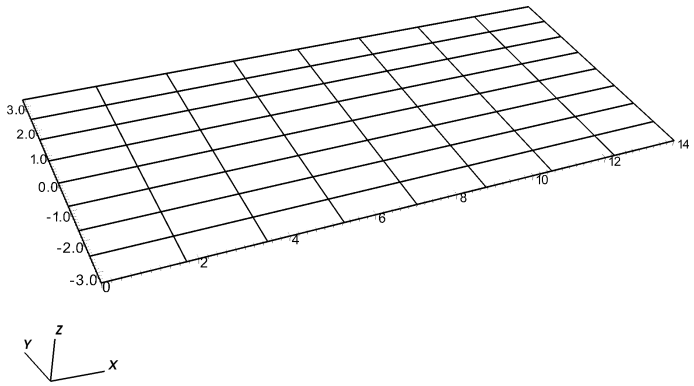

Figure 4.1: Geometry and finite element mesh with 512 elements.

In order to approximate the velocity we used 14739 unknowns, for temperature and pressure

729 unknowns each. The mesh size is $h_x = 1.75 \times 10^6 m, h_y = 0.825 \times 10^6 m, h_z = 0.5 \times 10^3 m$. The size of the time step is $\Delta t = 1$ day. The simulation time for $T = 50$ days is around 5 minutes and for $T = 365$ days is around 30 minutes.

4.2. Numerical simulations for Case 1. In the first set of computations, we use $T = 50$ days and the boundary conditions described in Section 2.3. Our findings are displayed in Figure 4.2 and Figure 4.3, which show the velocity at the surface at five different days. Since the temperature at the surface changes a little only, we give the average values of the temperature on the sea surface in Table 4.2. We notice that there is a relative high interpolation error of the initial temperature profile (Figure 2.2) due to the relative coarse finite element mesh. However, the principal effects of varying temperatures across the ocean depth can be accounted for in our three-dimensional model.

day 1	day 13	day 27	day 38	day 50
23.04°	25.53°	26.14°	27.39°	30.52°

Table 4.2: Temperature Case 1.

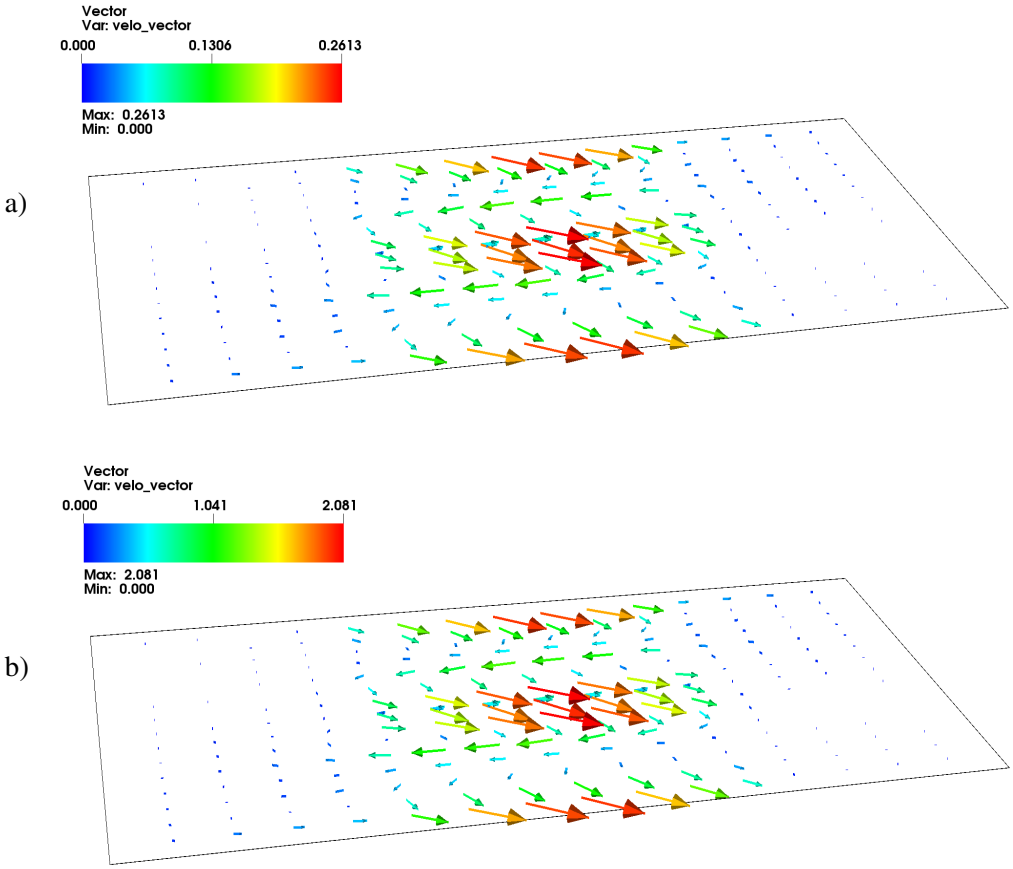

Figure 4.2: Velocity Case 1 at a) day 1 , b) day 13.

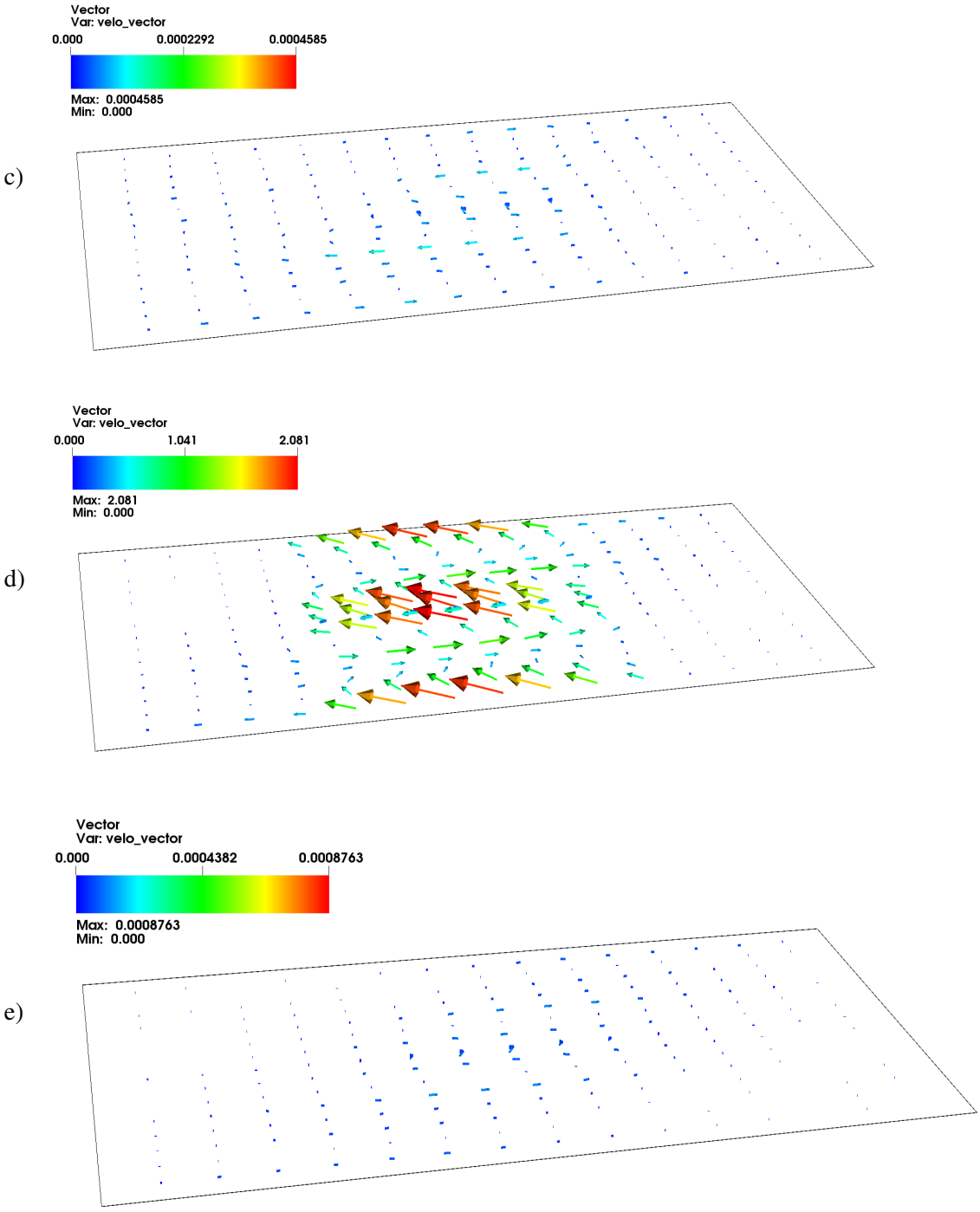

Figure 4.3: Velocity Case 1 at c) day 25, d) day 38 e) day 50.

4.3. Numerical simulations for Case 2. In the second set of simulations we consider a time horizon of one year, i.e., $T = 365$ days. The velocity at the sea surface at five different days is shown in Figure 4.4 and Figure 4.5, and the average value of the temperature on the sea surface in Table 4.3. Furthermore, in Figure 4.6 and Figure 4.7, the temperatures at depth 500m are displayed. Specifically, the direct access to intermediate temperature distributions below the sea level is simple thanks to our three-dimensional model. Clearly, in comparison to homogenized models (e.g., [6, 7]), three-dimensional computations are more costly.

day 1	day 91	day 182	day 273	day 364
23.00°	26.03°	28.02°	26.25°	26.01°

Table 4.3: Temperature Case 2.

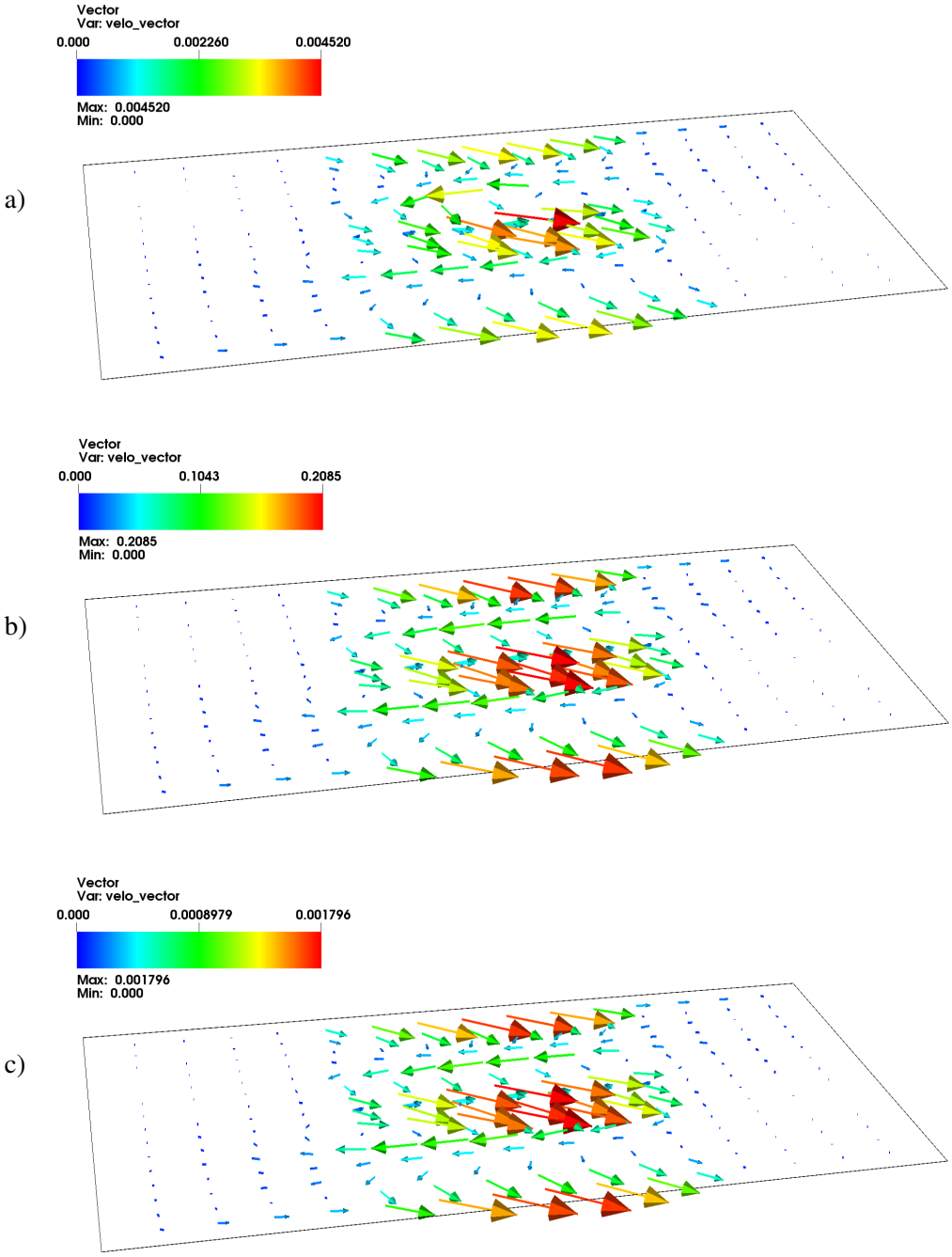

Figure 4.4: Velocity Case 2 at a) day 1, b) day 91 c) day 182.

d)

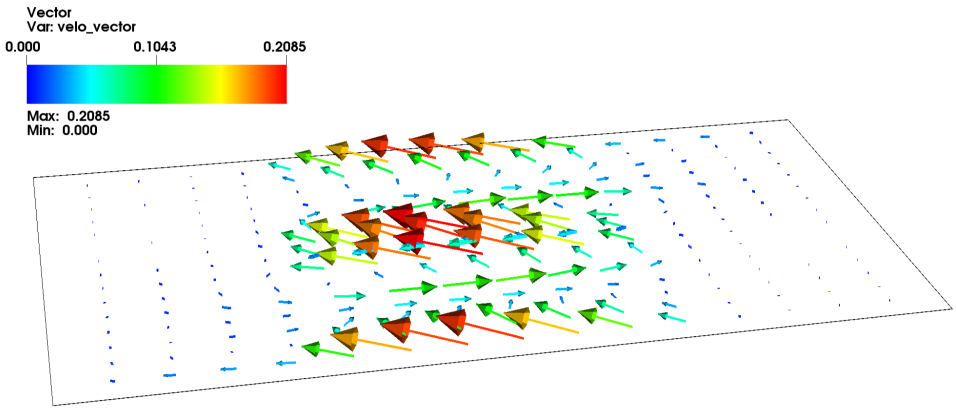

e)

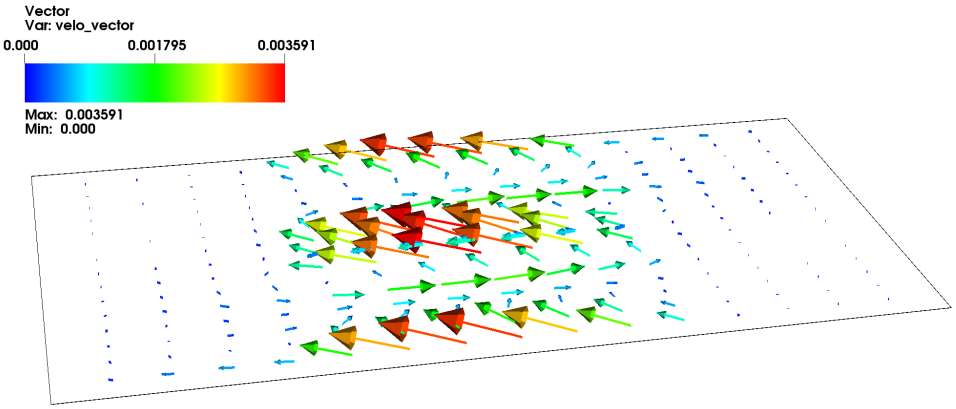

Figure 4.5: Velocity Case 2 at d) day 273, e) day 364.

a)

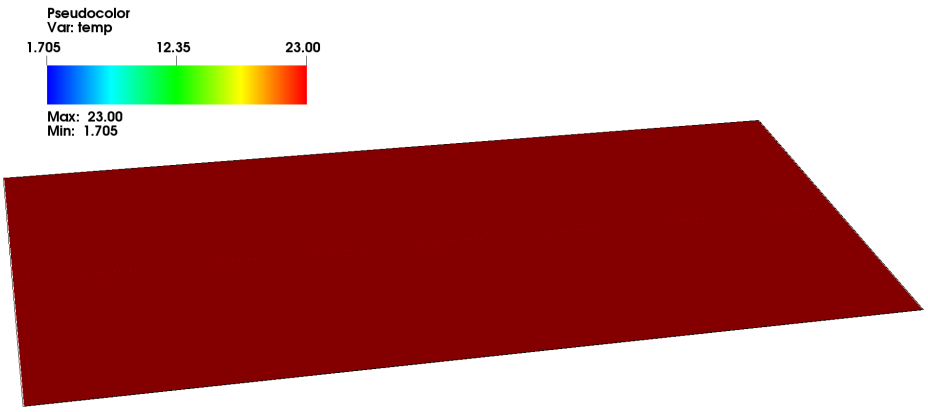

Figure 4.6: Case 2, Temperature at depth 500m at day 1.

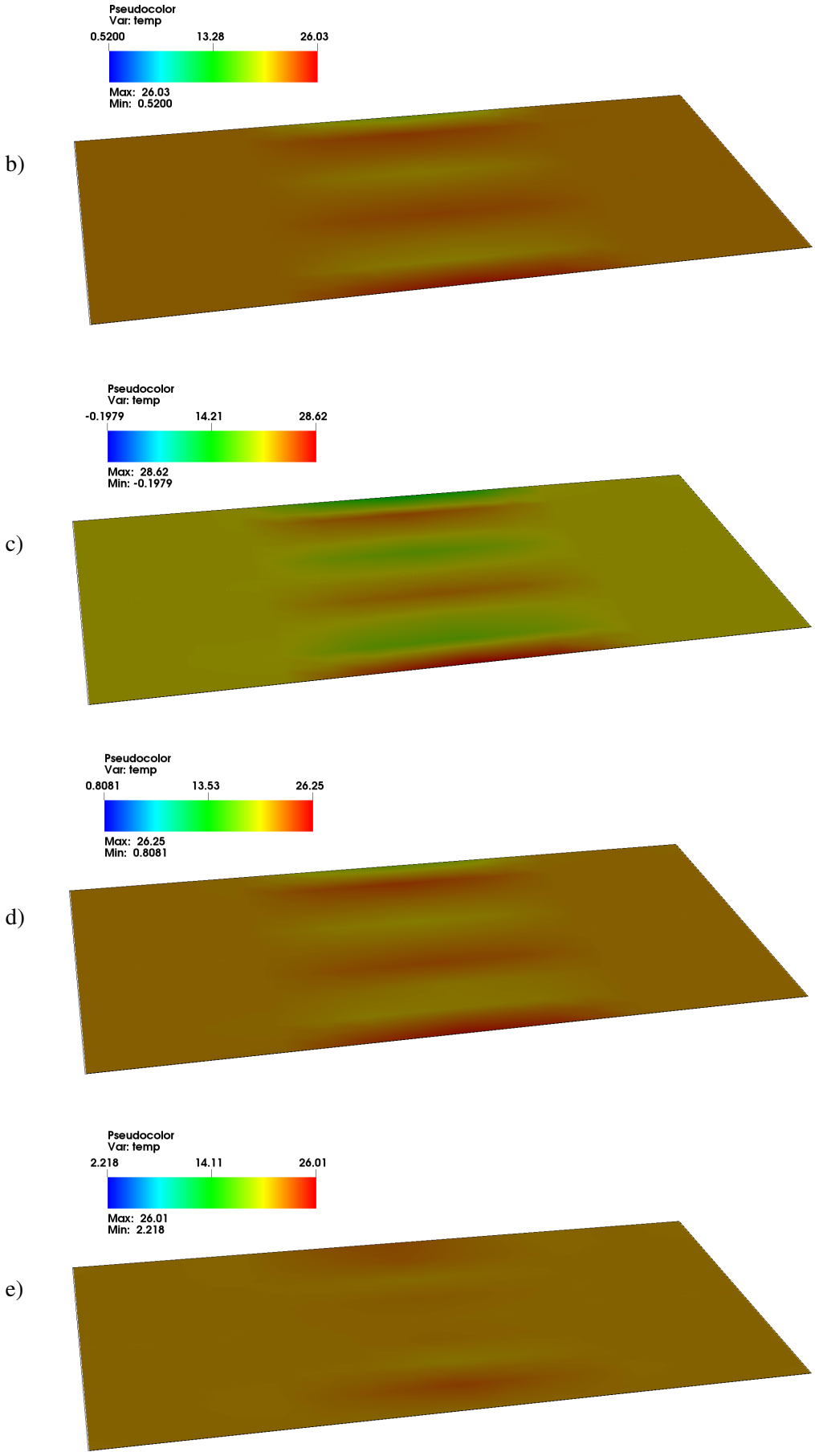

Figure 4.7: Case 2, Temperature at depth 500m at b) day 91, c) day 182, d) day 273 e) day 364.

5. Conclusions. In this work, we considered a simplified ocean model using the incompressible Navier-Stokes equations coupled to a temperature problem. Importantly, we used a three-dimensional formulation. Here, we derived a weak formulation and employed the Rothe method using a One-Step-θ scheme in time and Galerkin finite elements on a hexahedral mesh. The numerical solution was based on Newton's method. We carried out simulations for two different time horizons of 50 days and 365 days. The three-dimensional model allows us for an easy access of temperature (and velocity) values for different ocean depths. Ongoing work is on the implementation of a parallel solver to conduct mesh refinement studies. As future extensions, we plan to extend the model to include the atmosphere and the salinity and to employ an equation of state for non-constant densities.

Author contributions. The work carried out by the authors was equally distributed.

Funding. Did not receive financing.

Acknowledgment. The authors have been supported by the foundation Mathematik und Umwelt (mathematics and environment).

Conflicts of interest. "The authors declare no conflict of interest".

ORCID and License
Thomas Hartmann https://orcid.org/0009-0009-8837-5811
Ernst P. Stephan https://orcid.org/0000-0002-4069-6263
Thomas Wick https://orcid.org/0000-0002-1102-6332

References

[1] Clarke AJ. An Introduction to the Dynamics of El Nino and the Southern Oscillation. Academic Press; 2008.

[2] Sarachik ES, Cane MA. The El Nino-Southern Oscillation Phenomenon. Cambridge University Press; 2010.

[3] Cane MA. The response of an equatorial ocean to simple wind stress patterns: I. Model formulation and analytic results. Journal of Marine Research. 1979;37:233-52.

[4] Vallis GK. Atmospheric and Oceanic Fluid Dynamics. Cambridge: Cambridge University Press; 2017.

[5] Jin FF, Neelin JD. Modes of interannual tropical ocean–atmosphere interaction—a unfied view. Part I: Numerical results. Journal of the Atmospheric Sciences. 1993;50(21):3477-503.

[6] Lions JL, Temam R, Wang S. On the equations of the large-scale ocean. Nonlinearity. 1992 sep;5(5):1007. Available from: https://dx.doi.org/10.1088/0951-7715/5/5/002.

[7] Rubio O, Noriega R. A Mathematical Model for Oceanic Circulation at El Niño Phenomenon. Selecciones Matemáticas. 2018 Dec;5(02):249–264. Available from: https://revistas.unitru.edu.pe/index.php/SSMM/article/view/2201.

[8] Africa PC, Arndt D, Bangerth W, Blais B, Fehling M, Gassmöller R, et al. The deal.II Library, Version 9.6. Journal of Numerical Mathematics. 2024 Nov;32(4):369-80. Available from: https://www.degruyter.com/document/doi/10.1515/jnma-2024-0137/html.

[9] Wick T. Solving Monolithic Fluid-Structure Interaction Problems in Arbitrary Lagrangian Eulerian Coordinates with the deal.II Library. Archive of Numerical Software. 2013;1:1-19. Available from: https://media.archnumsoft.org/10305/.

[10] Hurlburt HE, Kindle JC, O'Brien JJ. A Numerical Simulation of the Onset of El Nino. Journal of Physical Oceanography. 1976;6(5):621–631. Available from: https://journals.ametsoc.org/view/journals/phoc/6/5/1520-0485_1976_006_0621_ansoto_2_0_co_2.xml.

[11] McCreary JP, Anderson DLT. Chapter 24 Simple Models of EL Niño and the Southern Oscillation. In: Nihoul JCJ, editor. Coupled Ocean-Atmosphere Models. vol. 40 of Elsevier Oceanography Series. Elsevier; 1985. p. 345–370. Available from: https://www.sciencedirect.com/science/article/pii/S0422989408707207.

[12] Latif M, Maier-Reimer E, Olbers DJ. Chapter 7 Climate Variability Studies with a Primitive Equation Model of the Equatorial Pacific. In: Nihoul JCJ, editor. Coupled Ocean-Atmosphere Models. vol. 40 of Elsevier Oceanography Series. Elsevier; 1985. p. 63–81. Available from: https://www.sciencedirect.com/science/article/pii/S0422989408707037.

[13] Wick T. Multiphysics Phase-Field Fracture: Modeling, Adaptive Discretizations, and Solvers. Berlin, Boston: De Gruyter; 2020. Available from: https://www.degruyter.com/view/title/523232.

[14] Girault V, Raviart PA. Finite Element method for the Navier-Stokes equations. Number 5 in Computer Series in Computational Mathematics. Springer-Verlag; 1986.